Article

Seismic Fragility Assessment of SMRFs Equipped with TMD Considering Cyclic Deterioration of Members and Nonlinear Geometry

Mohammad Reza Hemmati Khollari * [ID]**, Azita Asadi and Hamed Tajammolian**

Department of Civil Engineering, Yazd University, the University Blvd, Safayieh, Yazd 8915818411, Iran; aasadi@yazd.ac.ir (A.A.); h.tajammolian@yazd.ac.ir (H.T.)
* Correspondence: hemmati.mohammad93@gmail.com

Abstract: This paper presents seismic fragility curves to assess the effect of far-field ground motions on the behavior of high-rise steel moment resisting frame (SMRF) structures equipped with Tuned Mass Damper, considering the cyclic deterioration of members and P-Delta effect in the nonlinear region. For this purpose, three 8-, 20-, and 30-story SMRF structures are selected, 44 earthquake record sets are extracted from the FEMA P-695, Incremental Dynamic Analysis (IDA) is operated, and four structural damage states are considered through the framework of HAZUS, including slight, moderate, extensive, and complete. Maximum structural inter-story drift and floor acceleration are employed to quantify the damage states, and spectral acceleration is used as the intensity measure. Results show that the Tuned Mass Damper can reduce the probability of damage under earthquake excitation in all damage states for both structural and non-structural elements. The decline varies from 4.0% to 20.0%, depending on the ground motion intensity level, based on engineering demand parameters. Moreover, it is clear that nonlinear properties and component deterioration under cyclic excitation can affect structural response in all damage states, which concerns the obtained curves.

Keywords: tuned mass damper; nonlinear geometry; nonlinear incremental dynamic analysis; fragility curves; damage states; structural seismic assessment

1. Introduction

In recent decades, besides using lateral force resisting systems, civil engineers have consistently considered the utilization of modern devices such as vibration controller systems as an alternative to deal with earthquake and wind excitation, mitigate their vibration, and consequently improve the performance of the structures. Different controller systems are classified into passive, semi-active [1], active [2], and hybrid [3]. Tuned Mass Damper (TMD) is a device for passive control of structures subjected to earthquakes. It comprises a mass, a spring, and a damper attached to a structure to reduce its undesirable dynamic vibrations. In general, TMD's frequency is tuned with the fundamental mode of the structure, which is usually the first mode [4]. The straightforward design and operation of TMDs have led to the utilization of this type of damper in many high-rise buildings around the world, such as the Taipei 101 Tower in Taipei, Taiwan [5]; the CN Tower in Toronto, Canada [6]; the Millennium Bridge in London, UK; and the John Hancock Tower in Boston.

The TMD concept and its application basically return to the efforts made by Frahm [7]. Theories concerning TMD were later presented by Ormondroyd and Den Hartog [8,9]. Afterward, other researchers employed various approaches and developed these equations gradually. Randall et al. [10], Sadek et al. [11], Luong and Zhang [12], Warburton [13], Bekdaş et al. [14], Tsai and Lin [15], and Jin et al. [16] were among the most influential people who put much effort into the optimization of TMD's parameters. The idea of utilizing Multi Tuned Mass Dampers (MTMDs) has also been reviewed and expanded

recently. There is evidence that using MTMDs and optimizing their distribution, which involves taking a particular TMD for each structural mode, can be more effective than using a Single-Tuned Mass Damper [17–21].

With respect to the gradual change in the provisions approach from the force method to the performance-based method, it is essential to study the structural behaviors at different levels considering nonlinear geometry (P-Delta) and the deterioration of members in the nonlinear regions. As a result of large structural deformation caused by P-Delta effects, elements enter the nonlinear region, deterioration intensifies, and the structure collapses more rapidly [22]. In addition, providing reliable collapse assessments of structural systems under earthquake loading requires an analytical model that incorporates component deterioration in the strength and stiffness [23].

Structural performance levels are introduced using Engineering Demand Parameters (EDPs) through different guidelines, such as HAZUS [24]. These performance levels are shown via fragility curves. There have been numerous studies conducted over the past few years pertaining to fragility curves for lateral force-resisting and controller systems. Gaudio et al. [25] explained an analytical approach for seismic vulnerability evaluation of reinforced concrete structures at a large scale in which the inter-story drift was used as a demand parameter of the structure for damage estimation. By generating fragility curves, annual failure probabilities were calculated at particular damage states (DSs). The fragility curves of low-rise portal-framed industrial buildings were developed by Hao Qin et al. [26] for structural and non-structural elements exposed to tropical cyclone wind excitation. Cao et al. [27] proposed a consistent seismic hazard and fragility framework considering the combined capacity-demand uncertainties via the probability density evolution method, and a combined performance index with different assigned probabilities was well established. The approach indicated the combined efficiency and accuracy that provided an important basis for the subsequent research. Tajamolian et al. [28] simulated three-dimensional SMRFs supported on the TCFP base isolation considering different mass and stiffness eccentricity types in the plan and assessed the effect of base isolation on structural damages in different structural performance levels using the fragility curve. Zhang et al. [29] assessed the seismic fragility curves of masonry structures under aftershock conditions. They examined the effect of site condition, aftershock intensity, seismic wall area ratio, reinforced concrete tie column, number of stories, and mortar strength. A study conducted by Mashadi et al. [30] examined the impact of forward directivity pulses as well as the high-frequency components of near-fault earthquake records on the seismic performance of regular and irregular structures using fragility curves. The seismic fragility curves were also used by Borhan et al. [31] to investigate the performance of rotational-friction slip dampers in steel structures of varying heights. Using a damage distribution model, Li et al. [16] assessed the seismic capacity of damaged reinforced concrete columns after the main shock. Based on their findings, the degree of damage degree accumulated during main shocks and the axial load ratio of the columns had a significant effect on the collapse fragility index. Wong and Harris [32] evaluated seismic fragility curves of structures equipped with TMD based on plastic energy. By simulating SMRFs of 6-story buildings, they investigated the effect of TMD on the reduction of the input energy of the structure as well as the development of the fragility curve based on drift criterion in low DSs without consideration of P-Delta effects. Zhang et al. [33] studied the TMD effect on structures by evaluating a 20-story steel building equipped with TMD and considering soil-structure interaction effects. Although structural behavior and TMD effects in all regions were assessed in their study, the deterioration of components under cyclic loading—earthquake excitation—was not considered. This is while the structural strength and stiffness are dramatically degraded in nonlinear regions, and the results would be affected considerably.

As mentioned above, in recent studies, seismic fragility assessment of structures equipped with TMD has mainly been set with some imperfections, due to overlooking of component deterioration in the nonlinear zones or structural nonlinear geometry (P-Delta). Accordingly, it is important to study the impacts of TMD on structures with different heights

and nonlinear properties in all DSs, since the desired application of TMDs is more likely to be found in high-rise buildings with large deformations. The present study investigates the effect of TMD on structures in different DSs by simulating 8-, 20-, and 30-story buildings with SMRFs as lateral force-resisting systems and using the plastic hinge method to consider the deterioration of structural members in nonlinear zones along with considering P-Delta effects. In the framework of the FEMA P-695 [34], the seismic acceptability of models is evaluated and seismic performance factors are calculated. Performance levels are also achieved in the framework of HAZUS [24]. For these purposes, the finite element software OpenSEES [35] is used to model and analyze structures. Fragility, IDA, and pushover curves are drawn based on the results of the analysis.

2. Methodology

2.1. Performance-Based Design

The performance-based design method is used to evaluate structural behavior by focusing on structural operations in nonlinear regions. Standards define structural and non-structural damages based on EDPs by considering an appropriate intensity measure (IM). Earthquake intensity measures have different characteristics, and the studies by Kwong and Chopra [36,37], Ebrahimian et al. [38], and Grigoriu [39] showed that the appropriate IM depends on the considered EDP, the soil site characteristics, and structural frequency. In this study, spectral acceleration (S_a) is used as IM. Normally, this parameter is shown as $S_a(T_1, \xi)$. In this statement, T_1 is the first mod period and ξ is the structural damping.

Several EDPs have been suggested in articles and design codes for the assessment of seismic response, such as maximum floor acceleration [40], residual drift [41], maximum inter-story drift [42–44], and maximum inelastic displacement [45]. These EDPs reflect the extreme response of structures to earthquakes. As this study investigates the behavior of structural and non-structural elements under the main earthquakes in the framework of HAZUS [24], inter-story drift and floor acceleration are considered as the EDP. With respect to this guideline, the building's components are classified into structural elements sensitive to drift, non-structural elements sensitive to drift, and non-structural elements sensitive to acceleration. In addition, building DSs are categorized into four physical levels: slight, moderate, extensive, and complete. However, in this research, fragility curves in different DSs are presented for structural elements sensitive to drift and non-structural elements sensitive to acceleration. Table 1 presents the damage values in different DSs for these two cases for steel-framed high-rise buildings that are employed in this study [24].

**Table 1.** Damage measure values in four DSs (adapted from [24]).

|	DS			
	DS1	**DS2**	**DS3**	**DS4**
Peak floor acceleration	0.3 g	0.6 g	1.2 g	2.4 g
Maximum inter-story drift ratio	0.003	0.006	0.015	0.040

2.2. Modeling

A seismic evaluation of 8-, 20-, and 30-story structures with SMFs was carried out in this research. For each model, the effect of TMD on the reduction of floor displacement and acceleration with and without consideration of nonlinear geometry (P-Delta effects) was investigated separately, and the deterioration of components under cyclic loading—earthquake excitation—was considered using a modified Ibarra–Medina–Krawinkler deterioration model with Bilinear Hysteretic Response (Bilin material). Figures 1 and 2 show the typical plan and the elevation view of the seismic-force-resisting frame of 8-story buildings. The building's plans are cruciform, and the lateral force-resisting frames include three 6.1 m bays. In all buildings, the first floor is 4.6 m high, and the remaining floors are 4 m high. While the interior bays merely resist gravity forces, the perimeter bays also resist lateral forces. This fact, along with the symmetry of the buildings' plans, makes it possible to model and

analyze structures under earthquake excitation by selecting and analyzing only one of the lateral force-resisting bays (horizontal directional frame) as a representative of the whole structure. Geometric deformation effects caused by interior frames' gravity loads are also applied to the representative frame using the leaning column method (Figure 3).

The 8- and 20-story buildings were modeled and verified based on a paper from Elkady and Lignos [46]. This means, all components and their materials are selected based on this paper, and the presented curves are verified in accordance with it. The exact details of these models are presented in an article by Zareian et al. [18] and NIST GCR 10-917-8 [47]. In addition, 30-story models are loaded similarly to 8- and 20-story models, and their members are designed in ETABS software. Beam sections are W RBS, and column sections are W other-than-RBS. Structures are loaded based on ASCE 7-10 [48]. It should be noted that in loading, only dead and live loads and lateral loads caused by earthquake excitation are considered. Load combination of 1.05Dead + 0.25Live as effective seismic mass and load combination of 1.0Dead + 1.0Live as gravity load are applied to the frames. The 8- and 20-story buildings are designed based on ANSI/AISC 360-10 [49], and the 30-story buildings are designed based on ANSI/AISC 360-16 [50]. The response modification factor (R) for all structures is considered equal to 8. It is assumed that the buildings are located in California in the USA and are among the seismic design category D_{max}. Moreover, the soil site is stiff and categorized in class D of soil classification, and the buildings' occupancy is residential. The minimum specified yield stress for beams and columns is assumed to equal 345 Mpa, and the expected yield stress for beams is equal to 380 Mpa. Using Rayleigh's method, structural damping with an inherent damping ratio of two percent is taken into account. In order to simulate all the structures and perform the nonlinear static and dynamic analysis, OpenSEES [35] software is utilized.
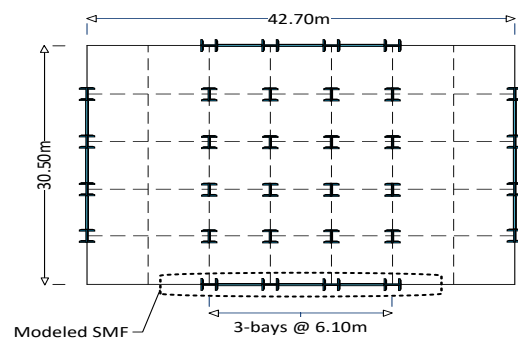
Figure 1. Typical view plan of the archetype structures (adapted with permission from [46]; Copyright 2014 John Wiley & Sons, Hoboken, NJ, USA).
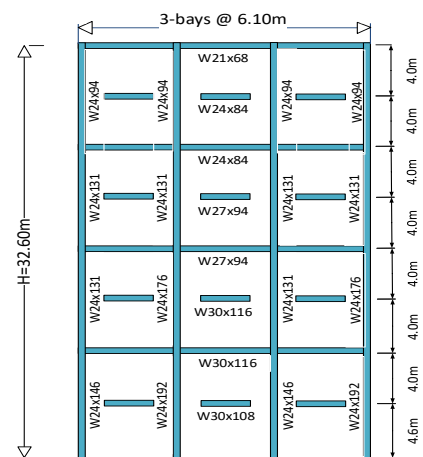
Figure 2. Elevation view of the 8-story SMF (adapted with permission from [46]; Copyright 2014 John Wiley & Sons, Hoboken, NJ, USA).
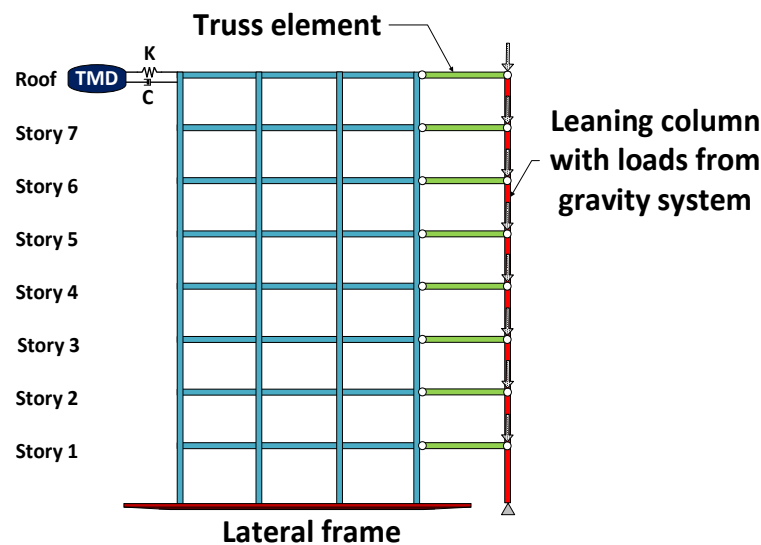
Figure 3. Illustration of leaning column and TMD.

To simulate nonlinear structural behavior, it is essential to consider nonlinear material properties and geometry (P-Delta effects). As structural behavior under earthquake excitation is cyclic, the nonlinear behavior of materials is simulated using deterioration models. In fact, correct evaluation of structural performance in different DSs, from serviceability to collapse, requires consideration of hysteresis models and participation of all the effective factors on the structures under the earthquake excitation. In this study, the plastic hinge method is used to simulate the nonlinear behavior of the beams and columns (Figure 4). In this method, elements are divided into the middle part, which includes elastic material, and the end parts in which inelastic material and the exact element's moment behavior are concentrated. The end regions can be simulated by nonlinear springs with unidirectional moment rotation behavior (M-θ) or a nonlinear discrete hinge. In this research, the concentrate hinge is simulated using nonlinear springs with bilinear hysteresis material, which was developed by Ibarra, Medina, and Krawinkler [51] (Figure 5). Relations of this material for box sections, W other-than-RBS and W RBS, were presented by Lignos and Krawinkler [23] through conducting more than 350 tests. Since, in these tests, the behavior of the plastic hinge is based on the natural behavior of the elements under real tests, local damages and deteriorations are regarded aptly. As an example, for the other-than-RBS beams that are used in this study, pre-capping plastic rotation for monotonic loading (θ_p), post-capping plastic rotation (θ_{pc}), and cumulative rotation capacity (Λ)—which is a parameter for considering the strength cyclic deterioration of components and is used in the modified Ibarra–Medina–Krawinkler deterioration model with Bilinear Hysteretic Response command given on the OpenSEES website—are as follows [23]:

$$\theta_p = 0.19 \cdot \left(\frac{h}{t_w}\right)^{-0.314} \cdot \left(\frac{b_f}{2 \cdot t_f}\right)^{-0.100} \cdot \left(\frac{L_b}{r_y}\right)^{-0.185} \cdot \left(\frac{L}{d}\right)^{0.113} \cdot \left(\frac{c^1_{unit} \cdot d}{533}\right)^{-0.760} \cdot \left(\frac{c^2_{unit} \cdot F_y}{355}\right)^{-0.0700} \tag{1}$$

$$\theta_{pc} = 9.52 \cdot \left(\frac{h}{t_w}\right)^{-0.513} \cdot \left(\frac{b_f}{2 \cdot t_f}\right)^{-0.863} \cdot \left(\frac{L_b}{r_y}\right)^{-0.108} \cdot \left(\frac{c^2_{unit} \cdot F_y}{355}\right)^{-0.36} \tag{2}$$

$$\Lambda = 585 \cdot \left(\frac{h}{t_w}\right)^{-1.14} \cdot \left(\frac{b_f}{2 \cdot t_f}\right)^{-0.632} \cdot \left(\frac{L_b}{r_y}\right)^{-0.205} \cdot \left(\frac{c^2_{unit} \cdot F_y}{355}\right)^{-0.391} \tag{3}$$

In Equations (1)–(3), F_y is the expected yield strength of the flange of the beam in megapascals and c^1_{unit} and c^2_{unit} are coefficients for unit conversion. They both are 1.0 if millimeters and megapascals are used. The parameter L_b is defined in this case as the distance from the column face to the nearest lateral brace, r_y is the radius of gyration about

the y-axis of the beam, L is the beam shear span, t_w is the web thickness, b_f is the width of the beam flange, t_f is the thickness of the beam flange, h is the web depth of the beam, and d is the beam depth.
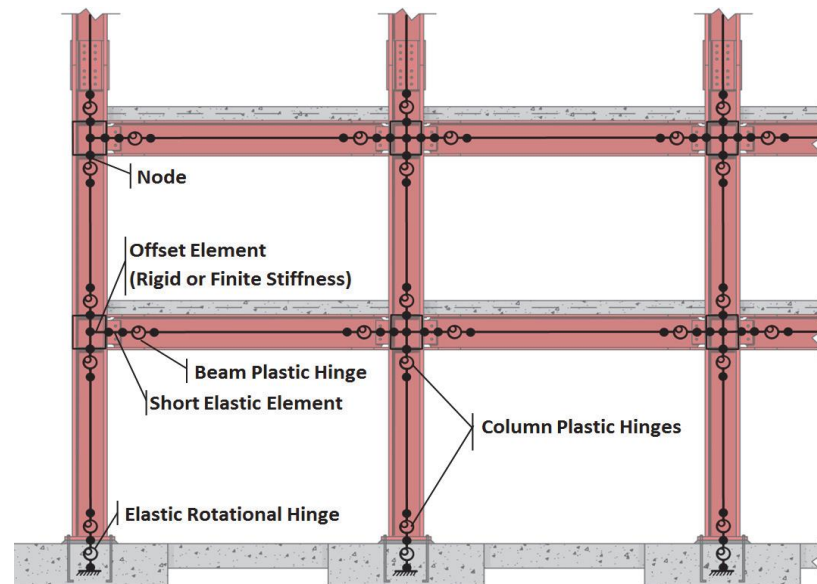

Figure 4. An idealized concentrated hinge centerline model for a typical SMRF (adapted from [52]).
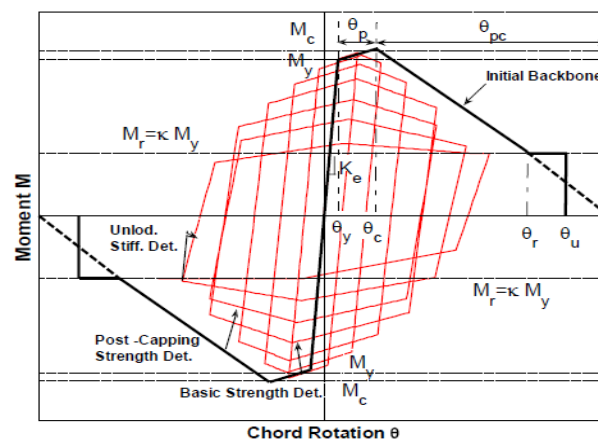

Figure 5. Modified Ibarra–Medina–Krawinkler deterioration material model (adapted from [35]).

It is necessary to combine lateral and gravity loads to model and analyze the nonlinear behavior of structures. The simultaneous existence of lateral and gravity loads on structures leads to nonlinear geometric behavior, known as the P-Delta effect. In this study, the P-Delta effect is applied to the columns of the lateral force-resisting frames. In addition, the P-Delta effects caused by interior frames are transformed via the leaning column to the representative frame. The leaning column is an element with two joints at both ends and is placed on the pinned support on the ground. Because this column only transforms P-Delta effects caused by gravity loads, its axial stiffness is infinite, and its moment stiffness is negligible. This column leans on a lateral force-resisting frame by means of rigid beams. These beams have a behavior similar to truss elements. They serve only to transform displacements in leaning columns to their corresponding nodes in the representative frame. Therefore, the axial stiffness of these beams is infinite (Figure 3).

Panel zones are also simulated, and their material is considered rigid. The Joint2D element is utilized to simulate the panel zone. This element contains a central spring and four perimeter springs in which the central spring has rigid material, representing the panel zone behavior. In addition, its perimeter springs are used to simulate bilinear material.

These perimeter springs have a moment rotation nonlinear unidirectional behavior (M-θ) and act exactly similar to zero-length elements (Figure 6).
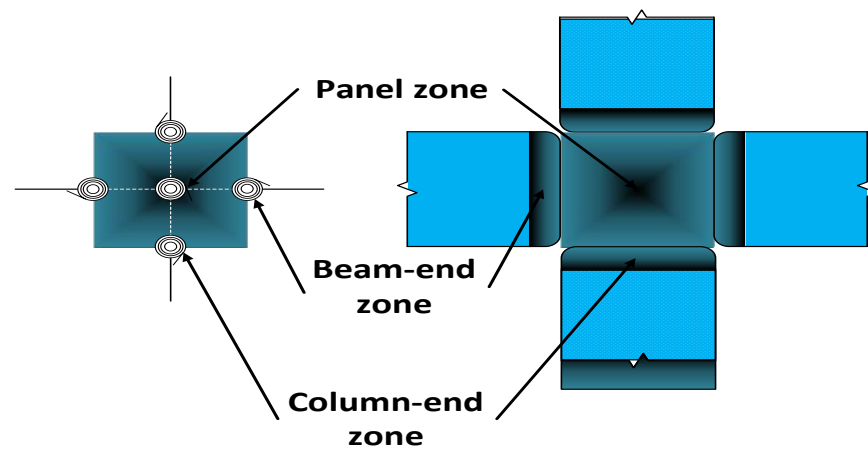
Figure 6. Idealized panel zone model (Adapted from Ref. [35]).

In order to simulate TMD, at first, an extra node is defined in the intended story, which is usually the roof story. TMD mass is usually considered between 2 to 5 percent of the structural effective seismic mass and is assigned to the defined node. In this study, the mass ratio is considered 2.5 percent. This node is joined to the roof node using a spring and viscose damper. The vertical and rotational displacement of these two nodes are tied to each other, and the horizontal displacement is released. By using the presented formulations in previous investigations, the intended stiffness and damping are assigned to the spring and the damper (Figure 3). In this research, the relations presented by Sadek et al. are used [11].

2.3. Ground Motion Record Set and IDA

One of the major uncertainty factors in structural seismic assessment is the frequency content of ground motions, which is idiomatically called record-to-record uncertainty. Aside from earthquake intensity, the structural response is also affected by the frequency content of the earthquake excitation. By using IDA, it is possible to consider record-to-record uncertainty.

To perform IDA, a Ground Motion Record Set (GMRS) is chosen and applied to the structure via one of the following algorithms: fixed-step or hunt-fill. In this study, the fixed-step algorithm was employed. At first, an appropriate IM was selected, then all the GMRSs were scaled to the same small intensity level. The ground motion intensity increased step by step until structures reached the collapse threshold [53]. According to the paper by Cornell and Vamvatsikos [54], the collapse threshold of structures in IDA is when the slope of the IDA curves is less than 20% of the initial slope.

Selecting a suitable GMRS needs some consideration, and it has been studied in different investigations [55,56]. In this study, the GMRS is taken from the FEMA P-695 (Table 2 [34]). This guideline categorizes GMRSs into two groups: far-field record sets and near-field record sets. The boundary between far-field and near-field record sets is considered 10 km from the rupture. In addition, this guideline introduces 22 pairs of GMRSs for far-field and 28 pairs for near-field to perform the IDA. In this study, structures are analyzed for far-field ground motions, so 22 pairs of GMRSs are selected; both horizontal components of an earthquake are presented in the FEMA P-695 [34]. The minimum distance of these records from the ground motion rupture (R_{Rup}) equals 11.1 km, and their maximum distance is 26.4 km. The magnitude of these ground motions is in the interval of 6.5 to 7.5 on the Richter scale, and the GPA of this GMRS varies from 0.21 g to 0.82 g.

Table 2. Characteristics of GMRS (adapted from [34]).

ID No.	Earthquake			Recording Station	
	M	**Year**	**Name**	**Name**	**Owner**
1	6.7	1994	Northridge	Beverly Hills—Mulhol	USC
2	6.7	1994	Northridge	Canyon Country-WLC	USC
3	7.1	1999	Duzce, Turkey	Bolu	ERD
4	7.1	1999	Hector Mine	Hector	SCSN
5	6.5	1979	Imperial Valley	Delta	UNAMUCSD
6	6.5	1979	Imperial Valley	EL Centro Array #11	USGS
7	6.9	1995	Kobe, Japn	Nishi-Akashi	CUE
8	6.9	1995	Kobe, Japn	Shin-Osaka	CUE
9	7.5	1999	Kocaeli, Turky	Duzce	ERD
10	7.5	1999	Kocaeli, Turky	Arcelik	KOERI
11	7.3	1992	Landers	Yermo Fire Station	CDMG
12	7.3	1992	Landers	Coolwater	SCE
13	6.9	1989	Loma Prieta	Capitola	CDMG
14	6.9	1989	Loma Prieta	Gilroy Array #3	CDMG
15	7.4	1990	Manjil, Iran	Abbar	BHRC
16	6.5	1987	Superstition Hills	El Centro lmp. Co.	CDMG
17	6.5	1987	Superstition Hills	Poe Road (temp)	USGS
18	7	1992	Cape Mendocino	Rio Dell Overpass	CDMG
19	7.6	1999	Chi-Chi Taiwan	CHY101	CWB
20	7.6	1999	Chi-Chi Taiwan	TCU045	CWB
21	6.6	1971	San Fernando	LA—Hollywood Stor	CDMG
22	6.5	1976	Friuli, Italy	Tolmezzo	. . .

3. Seismic Performance Evaluation of the Models

Using pushover and IDA curves, this study evaluated the seismic acceptability of structures under earthquake excitation within the framework of the FEMA P-695 [34]. The seismic performance factors of lateral-force-resisting systems were calculated; these consist of the response modification factor (R), overstrength system factor (Ω_0), and deflection amplification factor (C_d).

3.1. Modal and Pushover Analysis

According to the modal analysis of the models, the first mode period, T1, for the 8-, 20-, and 30-story structures is, respectively, 2.02, 3.96, and 6.22 s. According to the FEMA P-695 [34], the transition period, T_s, determines the boundary between short- and long-period structures. 0.6 s is the value of this parameter for structures in the D_{max} seismic design category. Therefore, all models are long periods. Using ASCE 7-10 [48] equations, the approximate fundamental building period, T, for the models is 1.65 s, 3.4 s, and 4.69 s, respectively. These values are shown in Table 3. The first mode shape is used to distribute the lateral load in the elevation of the structures for pushover analysis. The pushover curves are used to calculate the system overstrength factor and maximum nonlinear structural deformation.

The overstrength factor (Ω) is equal to the maximum base shear (V_{max}) divided by the design base shear (V). A structural nonlinear displacement is also described by period-based ductility (T), which is defined as the ratio of the ultimate roof drift displacement (δ_u)

to the effective yield roof drift displacement ($\delta_{y,eff}$). The ultimate roof drift displacement is considered equal to the drift corresponding to 80% of the maximum base shear capacity.

Table 3. Comparison of pushover parameters for 8-, 20-, and 30-story SMF structures, with (w) and without (w/o) considering P-Delta effects.

Number of Stories	With or without Consideration of P-Delta Effect	Ω	μ_T	$\frac{V_{max}}{W}$	$\frac{V}{W}$	T (s)	T_1 (s)
8	w/o P-Delta	2.98	6.25	0.135	0.045	1.65	2.02
	w P-Delta	2.66	4.94	0.121			
20	w/o P-Delta	3.34	3.90	0.073	0.022	3.40	3.95
	w P-Delta	2.87	2.58	0.063			
30	w/o P-Delta	4.36	5.01	0.069	0.016	4.69	6.22
	w P-Delta	3.36	2.38	0.054			

The values of these parameters for all simulated structures are calculated and presented in Table 3. In addition, the pushover curves for all 8-, 20-, and 30-story structures, with and without consideration of the P-Delta effect, are illustrated in Figure 7a–c. In these figures, the horizontal axes are the roof drift ratio, and the vertical axes are the normalized base shear force. According to Figure 7 and Table 3, the P-Delta effect causes a decrease in the system overstrength factor and period-based ductility. An 8-story building, for instance, has an overstrength factor of 2.98 when P-Delta is not taken into account and 2.66 when P-Delta is considered. For the 30-story building, period-based ductility is 2.38 if the P-Delta effect is taken into account and 5.01 if it is not. Moreover, it is clear that as the structure's height is raised, the period-based ductility decreases, and the overstrength factor increases. As an example, the period-based ductility of 8- and 20-story buildings considering the P-Delta effect is 4.54 and 2.58, respectively, and the overstrength factor is 2.66 and 2.87.
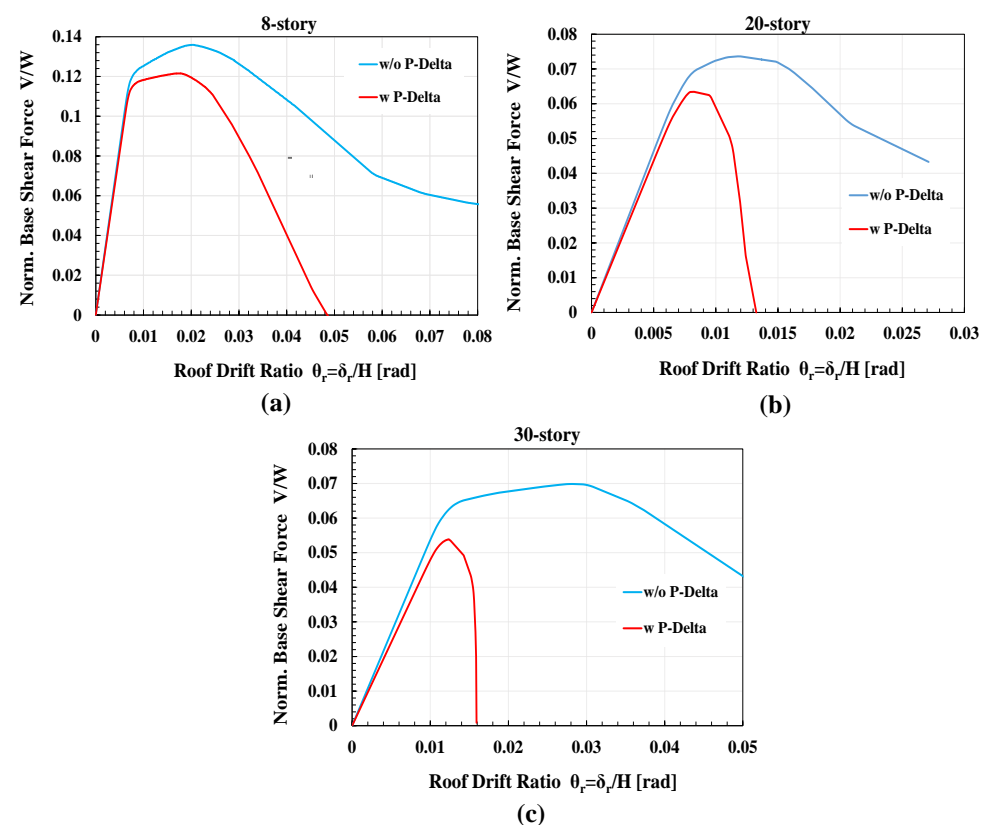
Figure 7. Comparison of pushover curves with (w) and without (w/o) consideration of the P-Delta effect: (**a**) 8-story, (**b**) 20-story, and (**c**) 30-story structures.

3.2. IDA Curves

In accordance with the FEMA P-695 [34], the seismic acceptability of structures is assessed, and the proper R factor is estimated using IDA curves. To accomplish this goal, besides considering effective uncertainty factors for simulation and structural analysis, parameters such as the median collapse intensity ($\hat{S}_{CT}$), the collapse margin ratio (CMR), and the adjusted collapse margin ratio (ACMR) of structures must be calculated and assessed.

One of the most important subjects in uncertainty studies is gathering enough data and information from the system and considering uncertainty factors in the behavior of structures. Total system collapse uncertainty (β_{TOT}) is equal to the sum of the squares of design requirement-related collapse uncertainty (β_{DR}), test data-related collapse uncertainty (β_{TD}), modeling-related collapse uncertainty (β_{MDL}), and record-to-record collapse uncertainty (β_{RTR}). β_{TOT} is obtained using Equation (4) [34]:

$$\beta_{TOT} = \sqrt{\beta_{RTR}^2 + \beta_{DR}^2 + \beta_{TD}^2 + \beta_{MDL}^2} \qquad (4)$$

Based on the FEMA P-695 [34], the amounts of β_{DR}, β_{TD}, and β_{MDL} are assumed to be 0.1, 0.2, and 0.2, respectively. β_{RTR} varies for each structure, and its amount is equal to the standard deviation of data on the collapse threshold. The values of β_{RTR} for models are presented in Table 7, which is explained in detail in Section 4. In addition, Table 4 shows the approximate values of β_{TOT}. This factor is employed to calculate the allowed adjusted collapse margin ratio (ACMR$_{all}$).

Table 4. Values of β_{TOT}.

Number of Stories	8	20	30
β_{TOT}	0.71	0.66	0.71

To assess the seismic acceptability of structures subjected to earthquake excitation, and to determine the appropriateness of the proposed R factor, two conditions must be taken into account [34]:

(1) Each performance group's average ACMR value exceeds ACMR$_{10\%}$, and the individual ACMR values for each index archetype within a performance group all exceed ACMR$_{20\%}$.

$$\overline{ACMR} = SSF * \overline{CMR} \geq ACMR_{10\%} \quad , \quad ACMR = SSF * CMR \geq ACMR_{20\%} \qquad (5)$$

(2) MCE ground motions should have an average collapse probability of 10% or less across a performance group. The collapse probability of MCE ground motions should be 20% or less for each index archetype within a performance group.

$$\overline{P}(D_S \geq collapse \mid S_a) \leq 10\% \quad , \quad P(D_S \geq collapse \mid S_a) \leq 20\% \qquad (6)$$

SSF is the spectral shape factor in these equations, CMR is calculated by $\hat{S}_{CT}$ to ground motion intensity corresponding to MCE ground motion (S_{MT}). D_s is also the amount of damage based on the intended EDP.

Baker and Cornell [57] demonstrated that rare earthquakes, such as those belonging to the MCE, have a specific spectral shape that varies from the shape of the design spectrum utilized in ASCE/SEI 7-05 [58] structural design. In the FEMA P-695 [34], a CMR factor is multiplied by the SSF coefficient, and its amount is modified to consider the influence of spectral shape on rare earthquakes. SSF relies on the approximate fundamental building period (T), period-based ductility (μ_T), and seismic design category (SDC), and its amount is obtained through the FEMA P-695 (Tables 7-1a and 7-1b [34]).

According to ASCE 7-10 [48], the probability of structural collapse under earthquake excitations with the possibility of occurring less than 2% during the structural life serviceability should be less than 10%. This level of ground motion intensity is called maximum

considered earthquake (MCE) or rare earthquake. The MCE ground motion intensity value for long-period structures is calculated through Equation (7).

$$S_{MT} = \frac{S_{M1}}{T} \tag{7}$$

In Equation (7), S_{M1} is the spectral acceleration related to the long-period structures, and T is the approximate fundamental building period of the models, based on ASCE 7-10 [48]. It is notable that ASCE 7-10 [48] considers MCE intensity 1.5 times the designed earthquake.

$\hat{S}_{CT}$ is calculated by using the FEMA P-695 [34] definition. It is the least intensity in which the structure collapses under half of the GMRS. $\hat{S}_{CT}$ can be calculated using the IDA graphs or fragility curves in the collapse state. In accordance with HAZUS [24], the inter-story drift ratio for the structural collapse threshold of tall SMRFs structures with 8 stories or more is 4%. In Table 5, median collapse capacities for different states are calculated based on structural IDA curves. In addition, this table shows the SSF, S_{MT}, ACMR, CMR, and probability of structural collapse under MCE excitation.

Table 5. Comparison of MCE ground motion intensity, SSF, $\hat{S}_{CT}$, CMR, ACMR, and probability of collapse under MCE ground motion for simulated models in different states.

Number of Stories	With or without Consideration of P-Delta Effect	With or without TMD	S_{MT} (g)	SSF	$\hat{S}_{CT}$ (g)	CMR	ACMR
8	w/o P-Delta	w TMD	0.545	1.522	1.598	2.930	4.460
		w/o TMD			1.301	2.386	3.6326
	w P-Delta	w TMD		1.452	1.590	2.915	4.232
		w/o TMD			1.195	2.192	3.182
20	w/o P-Delta	w TMD	0.264	1.392	2.642	9.980	16.606
		w/o TMD			3.158	11.930	13.892
	w P-Delta	w TMD		1.282	2.150	8.124	10.416
		w/o TMD			1.887	7.129	9.221
30	w/o P-Delta	w TMD	0.191	1.455	2.927	15.263	22.215
		w/o TMD			2.662	13.882	20.205
	w P-Delta	w TMD		1.264	2.397	12.500	15.802
		w/o TMD			2.116	11.034	13.949

All simulated structures are located in the qualified limit by comparing structures' ACMR with allowed values, presented in FEMA P-695 Table 7-3 [34]. Similarly, the probability of structural collapse under MCE excitation is also placed within the permitted limit. Consequently, the considered R factor for structures is appropriate. Further, it is evident that the ACMR factor values for the structures differ significantly from the allowed values, and as the height of a structure increases, this difference becomes more apparent. If the P-Delta effect is taken into account, the factor for 8-, 20-, and 30-story structures equipped with TMD is 4.232, 10.416, and 15.802, respectively. Thus, as structures get taller, the likelihood of structural damage from MCE excitation significantly decreases. The effects of TMD on structures are also evident. By adding TMD to structures, the ACMR factor increases, and as a result, the probability of structural collapse decreases. For example, the 20-story building with and without TMD considering the P-Delta effect has ACMR factors of 10.416 and 9.221, respectively. Moreover, the P-Delta effect decreases the ACMR factor and increases the probability of structural collapse under MCE excitation, as shown in Table 5. For a 30-story structure equipped with TMD, the ACMR factor with and without consideration of P-Delta effects is 15.802 and 22.215, respectively.

An example of IDA curves for 8-story structures considering the P-Delta effect and the deterioration of components under cyclic loading—earthquake excitation—with and without TMD is shown in Figure 8. Maximum inter-story drift is used as EDP in these graphs. The IDA graphs contain structural responses to 44 GMRS with varying intensities. Therefore, evaluating IDA curves and comparing them is difficult. To solve this problem, a good representation of each curve must be chosen. Generally, to compare IDA curves, fractile graphs are used. Fractiles 50, 16, and 84 represent the median structural responses and standard deviations of the IDA curve at each intensity level. This can provide a useful perspective on overall structural behavior and data dispersion. Figures 9–11 depict the fractile curves of 8-, 20-, and 30-story buildings for inter-story drift as EDP. By way of example, the 50th fractile curves of 8-story structures with the P-Delta effect indicate that a structure without TMD collapses at a level of approximately 1.0 g intensity. In contrast, it collapses at approximately 1.25 g when equipped with TMD.
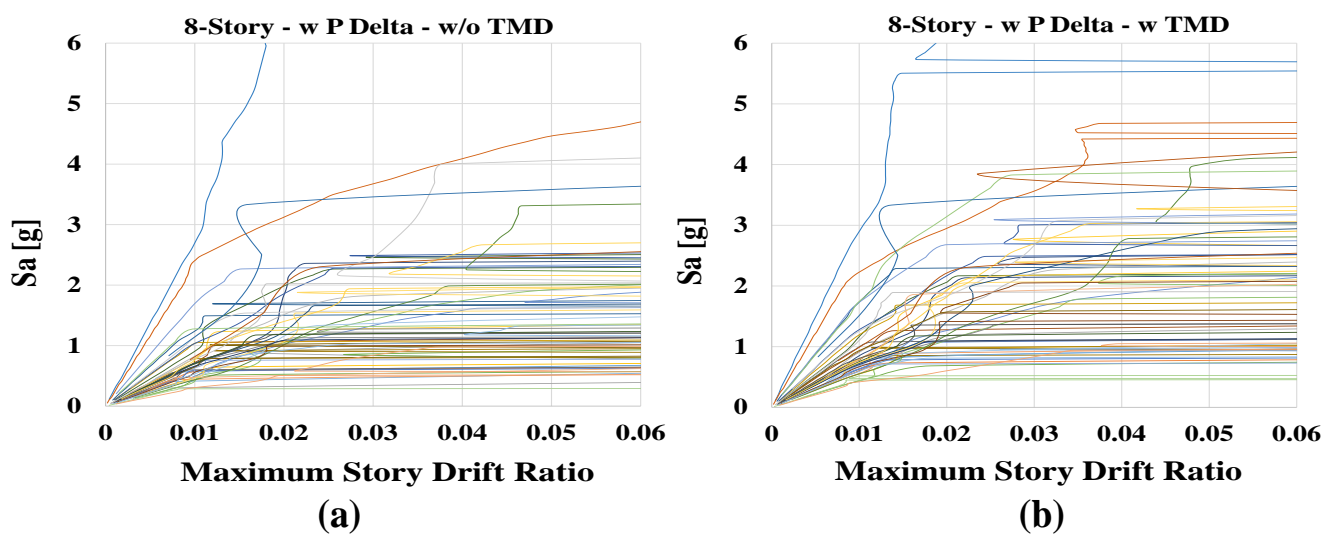

Figure 8. IDA response plot of spectral acceleration versus maximum inter-story drift ratio for 8-story structures with consideration of the P-Delta effect: (**a**) without (w/o) TMD, (**b**) with (w) TMD.
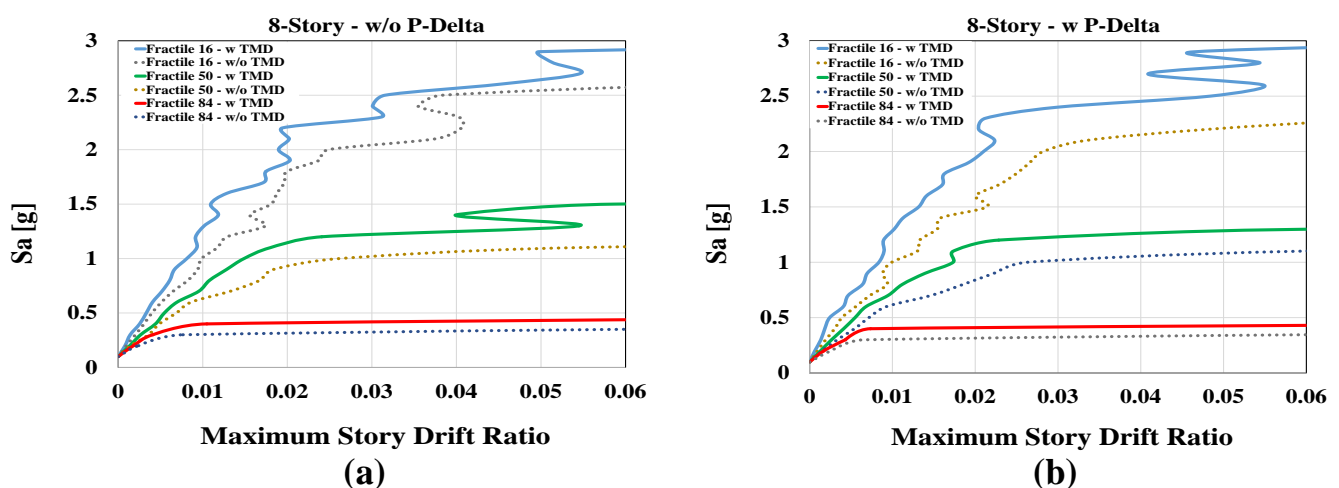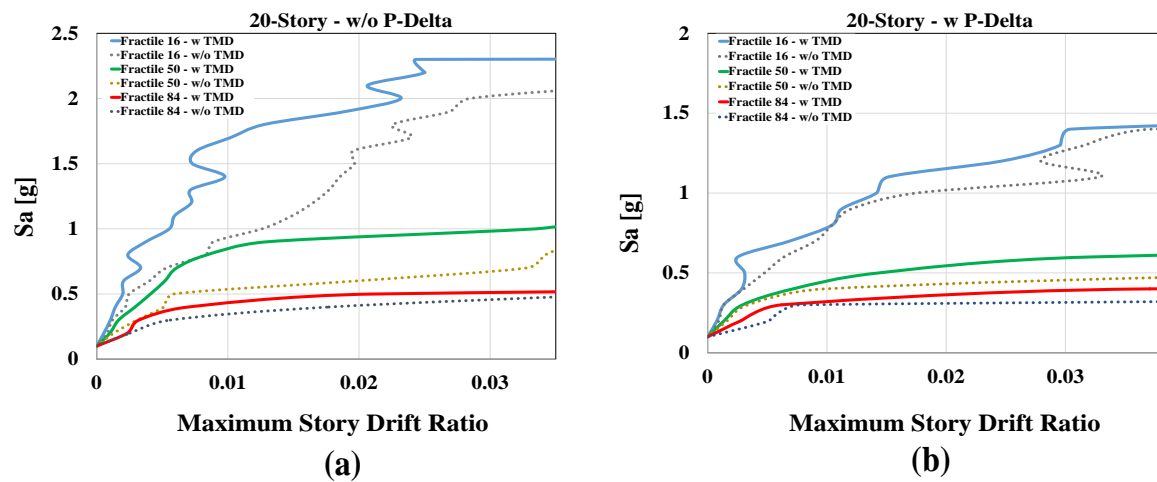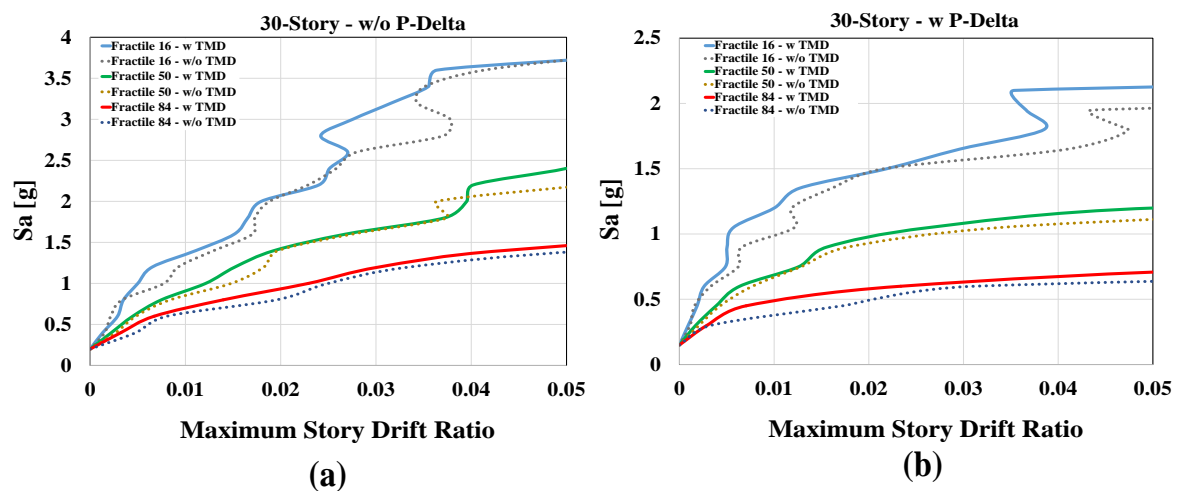

Figure 9. Fractiles 16, 50, and 84 of the IDA response of spectral acceleration versus maximum inter-story drift ratio for 8-story structures with (w) and without (w/o) TMD: (**a**) without consideration of the P-Delta effect, (**b**) with consideration of the P-Delta effect.

Figure 10. Fractiles 16, 50, and 84 of the IDA response of spectral acceleration versus maximum inter-story drift ratio for 20-story structures with (w) and without (w/o) TMD: (**a**) without consideration of the P-Delta effect, (**b**) with consideration of the P-Delta effect.

Figure 11. Fractiles 16, 50, and 84 of the IDA response of spectral acceleration versus maximum inter-story drift ratio for 30-story structures with (w) and without (w/o) TMD: (**a**) without consideration of the P-Delta effect (**b**) with consideration of the P-Delta effect.

4. Fragility Curves

The fragility curve implicitly addresses the uncertainty in earthquake demand caused by the spatial variability of ground motion. These curves for structural and non-structural drift and acceleration-sensitive components and each structural DS are drawn separately. Three steps are required to acquire fragility curves: conducting an IDA of the structures, determining the intended DSs, calculating the numerical probability of reaching or exceeding structural response to those DSs, and, finally, fitting lognormal curves to those numerical probabilities.

Normal cumulative distribution functions (CDFs) are commonly used to predict natural phenomena. CDFs are commonly used to predict natural phenomena. Because structural behavior is evaluated using natural data, this distribution function is presented in the lognormal form. Equation (8) shows the lognormal cumulative distribution function in standard form using HAZUS [24]:

$$P[d_s | S_a] = \Phi \left[\frac{1}{\beta_{ds}} \ln \left(\frac{S_a}{\bar{S}_{a,ds}} \right) \right] \tag{8}$$

where P is the probability of being in or exceeding a special DS in different earthquake intensity levels, d_s is the intended DS, S_a is the spectral acceleration as the intensity measure, Φ is the standard normal cumulative distribution function, β_{ds} is the standard deviation of the natural logarithm of spectral acceleration for DS, and $\overline{S}_{a,ds}$ is the median value of spectral acceleration at which the building reaches the threshold of DS.

Table 6 shows the values of $\hat{S}_{CT}$ for all DSs. According to this table, $\hat{S}_{CT}$ for all structures rises as the DS increases, and this issue is more significant in high DSs. As an example, in the 30-story structure equipped with TMD, the $\hat{S}_{CT}$ increases by 0.255 g in the slight DS to moderate DS but by 0.705 g in the moderate DS to extensive DS. In addition, the TMD effect on the growth of $\hat{S}_{CT}$ in all structural DSs is observable, which is also more considerable in high DSs. For example, in the complete DS in the 8-story structure, considering the P-Delta effect, the $\hat{S}_{CT}$ of structures with and without TMD is 1.577 g and 1.183 g, respectively. Similarly, in all structural DSs, the P-Delta effect causes a decrease in $\hat{S}_{CT}$. For instance, in the extensive DS in the 30-story structure equipped with TMD, the P-Delta effect causes a decrease in $\hat{S}_{CT}$ from 1.270 g to 1.215 g. Additionally, the $\hat{S}_{CT}$ increases with the height of structures. By way of example, in the complete DS, the $\hat{S}_{CT}$ of 8-, 20-, and 30-story structures equipped with TMD considering the P-Delta effect is 1.577 g, 2.116 g, and 2.497 g, in the same order.

Table 6. $\hat{S}_{CT}$ of the fragility curves in all the DSs.

| Number of Stories	8				20				30			
With or without Consideration of P-Delta Effect	w/o P-Delta		w P-Delta		w/o P-Delta		w P-Delta		w/o P-Delta		w P-Delta	
With or without TMD	w TMD	w/o TMD	w TMD	w/o TMD	w TMD	w/o TMD	w TMD	w/o TMD	w TMD	w/o TMD	w TMD	w/o TMD
$\hat{S}_{CT}$ in the slight DS (g)	0.253	0.212	0.251	0.209	0.243	0.215	0.241	0.212	0.265	0.221	0.255	0.215
$\hat{S}_{CT}$ in the moderate DS (g)	0.507	0.426	0.503	0.419	0.485	0.429	0.482	0.423	0.530	0.442	0.510	0.430
$\hat{S}_{CT}$ in the extensive DS (g)	1.163	0.900	1.153	0.888	1.143	0.990	1.129	0.975	1.270	1.075	1.215	1.035
$\hat{S}_{CT}$ in the complete DS (g)	1.582	1.249	1.577	1.183	2.490	1.950	2.116	1.874	2.991	2.639	2.497	2.162

Table 7 presents the values of standard deviation for all DSs. According to this table, TMD reduces the standard deviation. For example, in the complete DS in the 8-story structure, considering the P-Delta effect, the standard deviation with and without TMD is 0.557 and 0.650, respectively.

**Table 7.** Standard deviation of the fragility curves in all the DSs.

Number of Stories	8				20				30			
With or without Consideration of P-Delta Effect	w/o P-Delta		w P-Delta		w/o P-Delta		w P-Delta		w/o P-Delta		w P-Delta	
With or without TMD	w TMD	w/o TMD	w TMD	w/o TMD	w TMD	w/o TMD	w TMD	w/o TMD	w TMD	w/o TMD	w TMD	w/o TMD
Standard deviation in the slight DS	0.437	0.450	0.443	0.462	0.377	0.401	0.382	0.404	0.460	0.490	0.470	0.500
Standard deviation in the moderate DS	0.438	0.452	0.444	0.463	0.378	0.406	0.386	0.412	0.462	0.491	0.473	0.502
Standard deviation in the extensive DS	0.519	0.527	0.493	0.547	0.423	0.435	0.419	0.423	0.470	0.500	0.480	0.521
Standard deviation in the complete DS	0.603	0.633	0.557	0.650	0.605	0.622	0.525	0.586	0.640	0.670	0.640	0.660

For all DSs, Figures 12–17 illustrate the TMD effect on the fragility curves for structural elements sensitive to drift and non-structural elements sensitive to acceleration. Moreover, Tables 8 and 9 compare the probability of damage at some intensity levels for different DSs based on the presented curves (these intensity levels were selected randomly). For example, in the slight DS and the intensity level of 0.3 g, the probability of damage to structural elements sensitive to drift in the 8-, 20-, and 30-story structures decreased by 19.0%, 11.0%, and 13.5%, in the same order. This effect is also apparent in high DSs. For instance, in the extensive DS and the intensity level of 1.0 g, the probability of damage to structural elements sensitive to drift in the 8-, 20-, and 30-story structures decreased by 16.0%, 11.0%, and 14.0%, respectively. Likewise, in the complete DS and the intensity level of 1.7 g, the probability of damage to structural elements sensitive to drift in the 8-, 20-, and 30-story structures declined by 16.0%, 11.0%, and 9.5%, respectively.
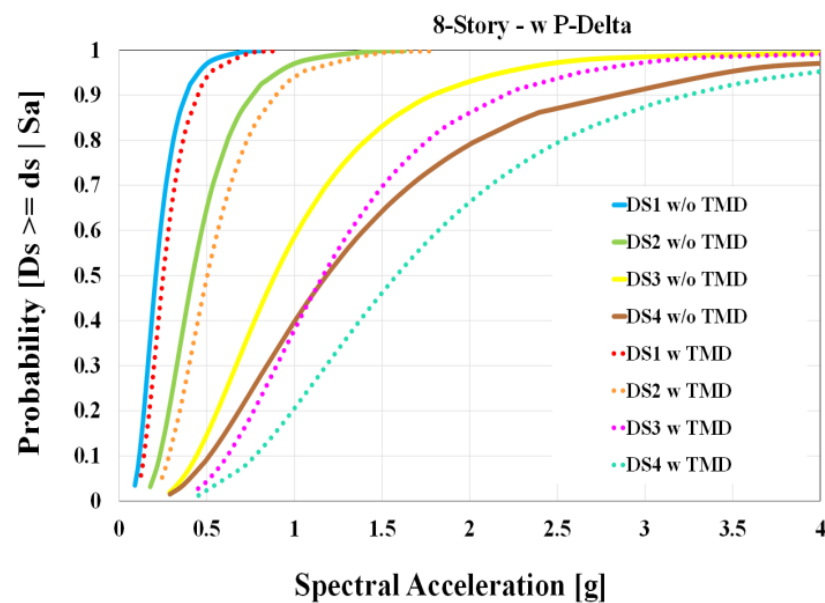
Figure 12. Fragility curves for the structural elements sensitive to the inter-story drift ratio of the investigated 8-story structures considering the P-Delta effect, with (w) and without (w/o) TMD.
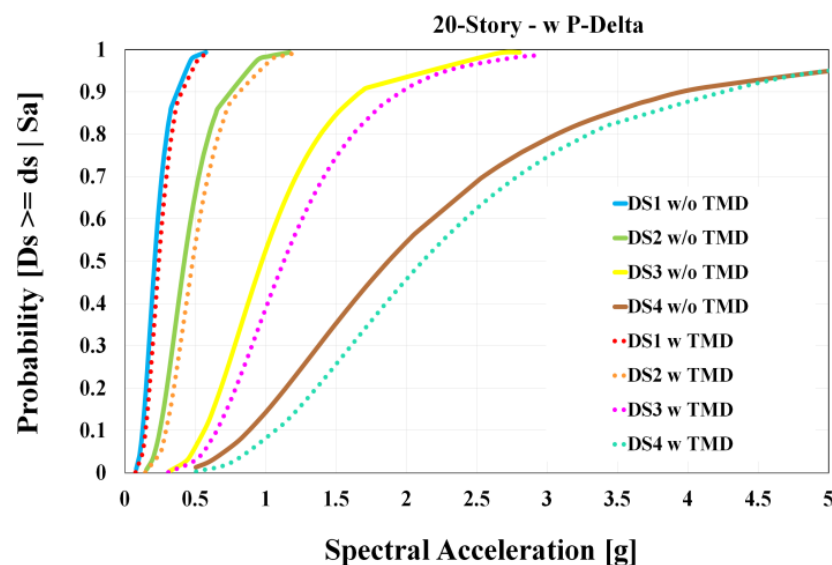
Figure 13. Fragility curves for the structural elements sensitive to the inter-story drift ratio of the investigated 20-story structures considering the P-Delta effect, with (w) and without (w/o) TMD.
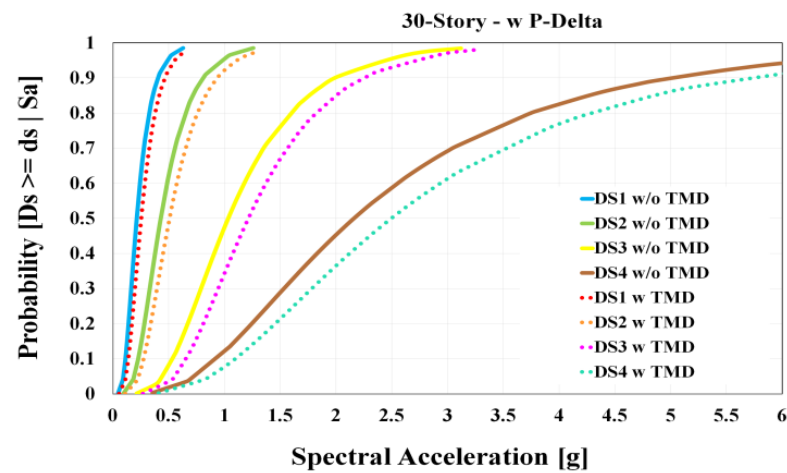
Figure 14. Fragility curves for the structural elements sensitive to the inter-story drift ratio of the investigated 30-story structures considering the P-Delta effect, with (w)and without (w/o) TMD.
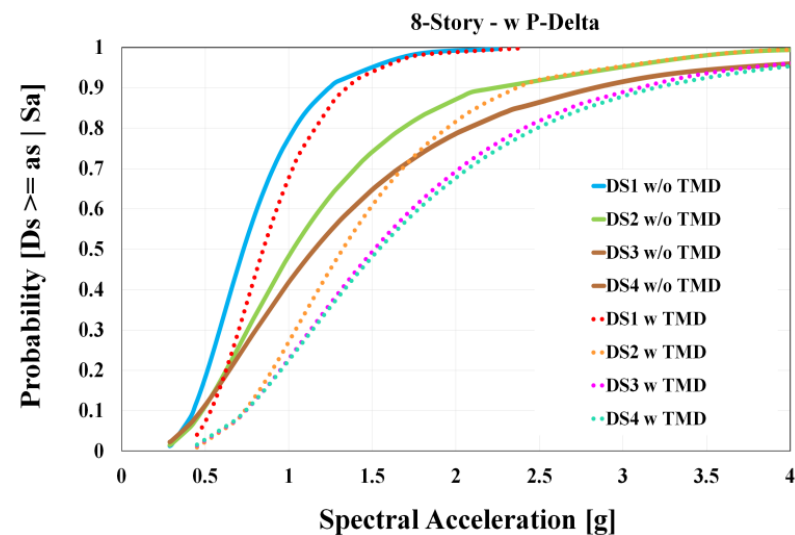

Figure 15. Fragility curves for the non-structural elements sensitive to the floor acceleration of the investigated 8-story structures considering the P-Delta effect, with (w) and without (w/o) TMD.
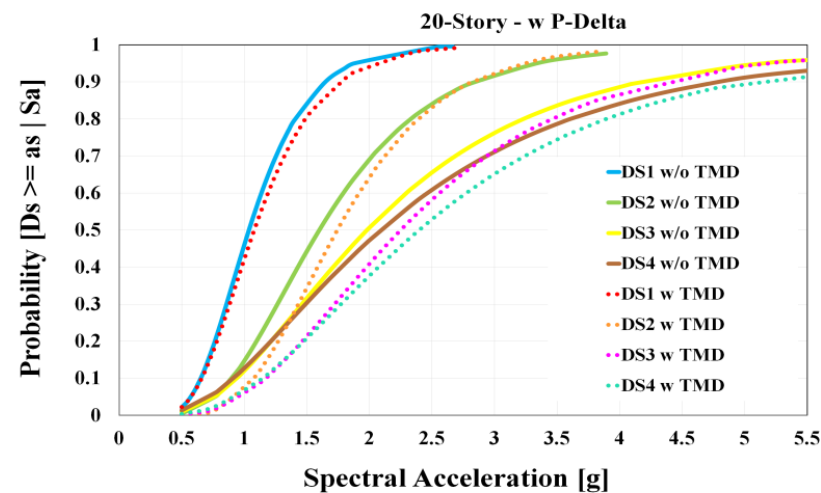

Figure 16. Fragility curves for the non-structural elements sensitive to the floor acceleration of the investigated 20-story structures considering the P-Delta effect, with (w) and without (w/o) TMD.
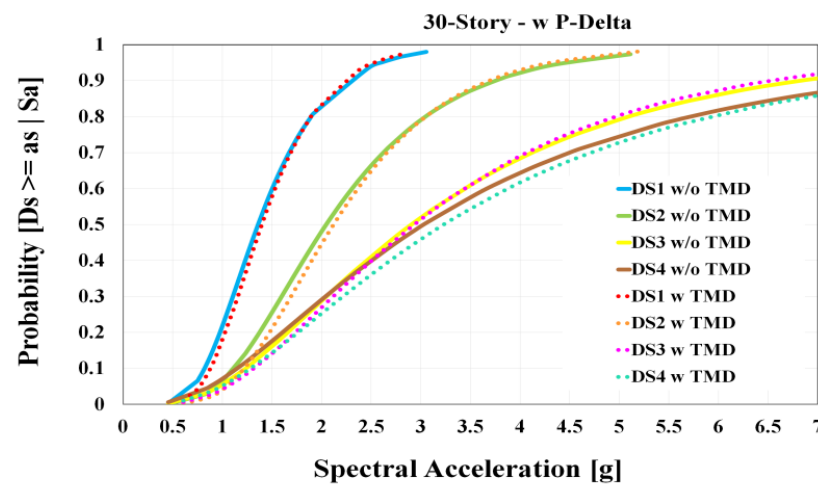
Figure 17. Fragility curves for the non-structural elements sensitive to the floor acceleration of the investigated 30-story structures considering the P-Delta effect, with (w) and without (w/o) TMD.

Table 8. TMD effect on the reduction of the probability of damage at some random ground motion intensity levels for structural elements sensitive to drift.

| Damage State	Number of Stories	Ground Motion Intensity Level (g)	Probability of Damage w/o TMD (%)	Probability of Damage w TMD (%)	TMD Effect (%)
Slight	8	0.3	79	60	19
	20	0.3	82	71	11
	30	0.3	76	62.5	13.5
Moderate	8	0.5	67	50	17
	20	0.5	68	55	13
	30	0.5	62	48	14
Extensive	8	1.0	54	38	16
	20	1.0	53	42	11
	30	1.0	48	34	14
Complete	8	1.7	71	55	16
	20	1.7	44	33	11
	30	1.7	36	26.5	9.5

Table 9. TMD effect on the reduction of the probability of damage at some random ground motion intensity levels for non-structural elements sensitive to acceleration.

Damage State	Number of Stories	Ground Motion Intensity Level (g)	Probability of Damage w/o TMD (%)	Probability of Damage w TMD (%)	TMD Effect (%)
Slight	8	1.0	81.0	68.0	13.0
	20	1.0	48.5	42.0	6.5
	30	1.0	26.4	21.7	4.7
Moderate	8	1.2	61.0	41.0	20.0
	20	1.2	26.0	16.0	10.0
	30	1.2	13.8	9.4	4.4
Extensive	8	2.0	79.0	69.0	10.0
	20	2.0	50.5	40.5	10.0
	30	2.0	29.1	28.5	1.1
Complete	8	2.5	86.5	80.0	6.5
	20	2.5	61.0	53.0	8.0
	30	2.5	39.9	36.4	3.5

The effect of TMD on the non-structural elements sensitive to acceleration is also considerable. For instance, in the moderate DS and the intensity level of 1.2 g, the probability of damage to non-structural elements due to floor acceleration of 8-, 20-, and 30-story structures decreased by 20.0%, 10.0%, and 4.4%, respectively. In addition, in the complete DS and the intensity level of 2.5 g, the probability of damage to non-structural elements due to floor acceleration of 8-, 20-, and 30-story structures declined by 6.5%, 8.0%, and 3.5%, in the same order.

Based on the presented curves, TMD is more effective in reducing inter-story drift in lower DSs, whereas in higher DSs it is more effective in reducing floor acceleration. In addition, as a result of the comparisons presented in Tables 8 and 9, it is possible to conclude that TMD can reduce the maximum inter-story drift and floor acceleration of structures from approximately 4.0% to 20.0%.

In addition to other curves, the moment-rotation curve illustrates the effects of TMD on the structural elements. Figure 18 illustrates the moment-rotation curves of some beams in the 8-, 20-, and 30-story structures under earthquake excitation (these beams were selected randomly). In Table 10, the effect of TMD on the rotation reduction of the mentioned beam is presented. As an example, the end beam rotation of the side span on the sixth floor of the 8-story building (considering the P-Delta effect) decreased by 7.61% under Lander's earthquake excitation and an intensity level of 1.36 g. Alternatively, considering the P-Delta effect and the intensity level of 3.35 g, with the Hector Mine earthquake excitation on the seventeenth floor of the 20-story building, the end beam rotation decreased by 19.86%. Similarly, the end beam rotation of the side span on the twenty-second floor of the 30-story building considering the P-Delta effect under the Duzce earthquake excitation and the intensity level of 2.32 g declined by 39.98%.
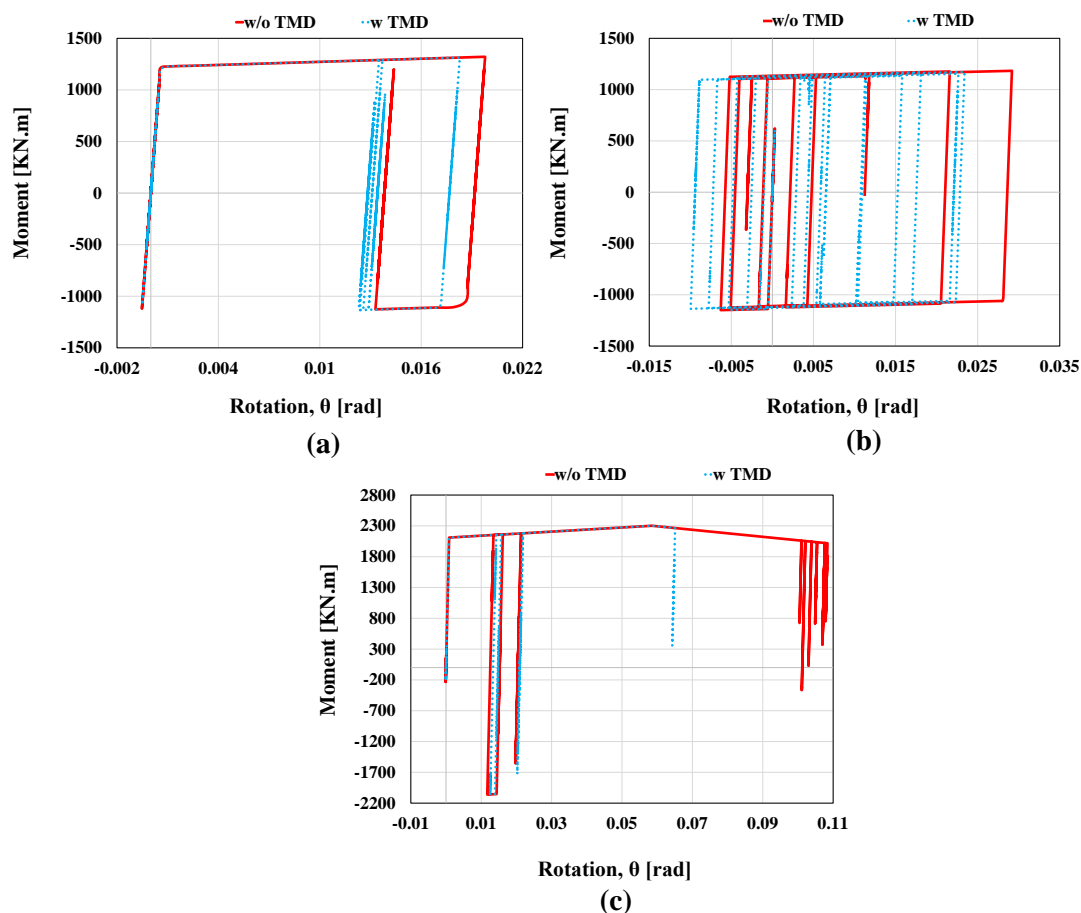
Figure 18. Moment rotation curve of some beams with (w) and without (w/o) TMD in the structures with consideration of P-Delta effect: (**a**) 8-story structure, (**b**) 20-story structure, and (**c**) 30-story structure.

Table 10. TMD effect on reduction of beam rotation in some random cases.

Number of Stories	Ground Motion Intensity Level (g)	Beam Rotation w/o TMD (rad)	Beam Rotation w TMD (rad)	TMD Effect (%)
8	1.36	0.0197	0.0182	7.61
20	3.35	0.0292	0.0234	19.86
30	2.32	0.1083	0.0650	39.98

5. Conclusions

The present study evaluated the performance and response of medium and tall buildings equipped with TMDs subjected to earthquake excitations. This investigation considers nonlinear structural geometry (P-Delta effects) and the deterioration of structural elements in load cycles in order to assess seismic performance and determine DSs using the frameworks of the FEMA P-695 [34] and HAZUS [24]. To accomplish this, OpenSEES [35]—the finite element software—was used to simulate and analyze 8-, 20-, and 30-story structures under IDA, and the results of this analysis were compared in different states. Following are summaries of the results of this study regarding the pushover, IDA, and fragility curves of the structures in different DSs, as well as the calculation of seismic performance factors:

1. TMD can increase ACMR values considerably. In addition, comparing the acquired ACMR with the values permitted by the FEMA P-695 [34], it is evident that the R factor presented in design codes such as ASCE 7-10 [48] for tall buildings is quite conservative and larger amounts can be used for SMFs.
2. It is imperative to take into account the nonlinear structural geometry (P-Delta effect) as well as the deterioration of structural elements during loading cycles to accurately simulate and analyze the structure in the nonlinear region.
3. A TMD can reduce the probability of damage under earthquake excitation not only at intermediate DSs such as slight and moderate but also at high DSs such as extensive and complete.
4. By considering the inter-story drift and maximum structural floor acceleration as the EDP, a TMD can reduce the probability of structural and non-structural damage from 4.0% to 20.0%.

6. Limitations and Future Works

This paper assesses the effect of TMD on SMRF structures under earthquake excitation via fragility curves. The efficiency and accuracy of simulated models and the used approach are verified by comparing the presented curves and results with valid papers and references. However, there are also significant issues and notes to be taken into account, which could lead to a new direction for investigation in the future.

1. In this study, a Single-Tuned Mass Damper concentrated on the structural roof is considered. The use of MTMDs and optimizing their distribution, which involves taking a specific TMD for each structural mode, will be more effective than Single-Tuned Mass Dampers.
2. In recent studies, new intensity measures such as average spectral acceleration ($S_{a,avg}$) for seismic response assessment of structures were introduced that seem more sophisticated than S_a.

Author Contributions: M.R.H.K.: software; formal analysis; writing—original draft; validation. A.A.: supervision; project administration; conceptualization; methodology. H.T.: methodology; data curation; writing—review and editing. All authors have read and agreed to the published version of the manuscript.

References

1. Renzi, E.; De Angelis, M. Optimal semi-active control and non-linear dynamic response of variable stiffness structures. *J. Vib. Control.* **2005**, *11*, 1253–1289. [CrossRef]
2. Soong, T.; Spencer, B., Jr. Supplemental energy dissipation: State-of-the-art and state-of-the-practice. *Eng. Struct.* **2002**, *24*, 243–259. [CrossRef]
3. Agrawal, A.; Tan, P.; Nagarajaiah, S.; Zhang, J. Benchmark structural control problem for a seismically excited highway bridge—Part I: Phase I problem definition. *Struct. Control Health Monit.* **2009**, *16*, 509–529. [CrossRef]
4. Elias, S.; Matsagar, V. Research developments in vibration control of structures using passive tuned mass dampers. *Annu. Rev. Control* **2017**, *44*, 129–156. [CrossRef]
5. Tuan, A.Y.; Shang, G. Vibration control in a 101-storey building using a tuned mass damper. *J. Appl. Sci. Eng.* **2014**, *17*, 141–156.
6. Sacks, M.P.; Swallow, J.C. Tuned mass dampers for towers and buildings. In *Structural Engineering in Natural Hazards Mitigation*; ASCE: Reston, VI, USA, 1993; pp. 640–645.
7. Frahm, H. Device for Dampin Vibration of Bodies. U.S. Patent US989958A, 18 April 1909.
8. Ormondroyd, J. The theory of the dynamic vibration absorber. *J. Appl. Mech.* **1928**, *50*, 9–22.
9. Den Hartog, J.P. *Mechanical Vibrations*; Courier Corporation: North Chelmsford, MA, USA, 1985.
10. Randall, S.; Halsted, D., III; Taylor, D. Optimum vibration absorbers for linear damped systems. *J. Mech. Des.* **1981**, *103*, 908–913. [CrossRef]
11. Sadek, F.; Mohraz, B.; Taylor, A.W.; Chung, R.M. A method of estimating the parameters of tuned mass dampers for seismic applications. *Earthq. Eng. Struct. Dyn.* **1997**, *26*, 617–635. [CrossRef]
12. Leung, A.Y.; Zhang, H.; Cheng, C.; Lee, Y. Particle swarm optimization of TMD by non-stationary base excitation during earthquake. *Earthq. Eng. Struct. Dyn.* **2008**, *37*, 1223–1246. [CrossRef]
13. Warburton, G. Optimum absorber parameters for minimizing vibration response. *Earthq. Eng. Struct. Dyn.* **1981**, *9*, 251–262. [CrossRef]
14. Bekdaş, G.; Nigdeli, S.M.; Yang, X.-S. A novel bat algorithm based optimum tuning of mass dampers for improving the seismic safety of structures. *Eng. Struct.* **2018**, *159*, 89–98. [CrossRef]
15. Tsai, H.C.; Lin, G.C. Optimum tuned-mass dampers for minimizing steady-state response of support-excited and damped systems. *Earthq. Eng. Struct. Dyn.* **1993**, *22*, 957–973. [CrossRef]
16. Li, L.; Chen, J.; Wang, W. Evaluation of the Residual Seismic Capacity of Post-Earthquake Damaged RC Columns Based on the Damage Distribution Model. *Buildings* **2023**, *13*, 595. [CrossRef]
17. Pellizzari, F.; Marano, G.; Palmeri, A.; Greco, R.; Domaneschi, M. Robust optimization of MTMD systems for the control of vibrations. *Probabilistic Eng. Mech.* **2022**, *70*, 103347. [CrossRef]
18. Zareian, F.; Lignos, D.; Krawinkler, H. Evaluation of seismic collapse performance of steel special moment resisting frames using FEMA P695 (ATC-63) methodology. In Proceedings of the Structures Congress 2010, Orlando, FL, USA, 15–15 May 2010; pp. 1275–1286.
19. Kleingesinds, S.; Lavan, O. Gradient-based multi-hazard optimization of MTMDs for tall buildings. *Comput. Struct.* **2021**, *249*, 106503. [CrossRef]
20. Frans, R.; Arfiadi, Y. Designing optimum locations and properties of MTMD systems. *Procedia Eng.* **2015**, *125*, 892–898. [CrossRef]
21. Domizio, M.; Garrido, H.; Ambrosini, D. Single and multiple TMD optimization to control seismic response of nonlinear structures. *Eng. Struct.* **2022**, *252*, 113667. [CrossRef]
22. Ibarra, L.F. *Global Collapse of Frame Structures under Seismic Excitations*; Stanford University: Stanford, CA, USA, 2004.
23. Lignos, D.G.; Krawinkler, H. Deterioration modeling of steel components in support of collapse prediction of steel moment frames under earthquake loading. *J. Struct. Eng.* **2011**, *137*, 1291–1302. [CrossRef]
24. HAZUS. *Multi-Hazard Loss Estimation Methodology, Earthquake Model HAZUS-MH MR5 Technical Manual*; Federal Emergency Management Agency: Washington, DC, USA, 2021.
25. Del Gaudio, C.; Ricci, P.; Verderame, G.; Manfredi, G. Development and urban-scale application of a simplified method for seismic fragility assessment of RC buildings. *Eng. Struct.* **2015**, *91*, 40–57. [CrossRef]
26. Qin, H.; Mason, M.; Stewart, M.G. Fragility assessment for new and deteriorated portal framed industrial buildings subjected to tropical cyclone winds. *Struct. Saf.* **2023**, *100*, 102287. [CrossRef]
27. Cao, X.-Y.; Feng, D.-C.; Beer, M. Consistent seismic hazard and fragility analysis considering combined capacity-demand uncertainties via probability density evolution method. *Struct. Saf.* **2023**, *103*, 102330. [CrossRef]
28. Tajammolian, H.; Khoshnoudian, F.; Rad, A.R.; Loghman, V. Seismic fragility assessment of asymmetric structures supported on TCFP bearings subjected to near-field earthquakes. *Structures* **2018**, *13*, 66–78. [CrossRef]
29. Zhang, Y.; Wang, Z.; Jiang, L.; Skalomenos, K.; Zhang, D. Seismic fragility analysis of masonry structures considering the effect of mainshock-aftershock sequences. *Eng. Struct.* **2023**, *275*, 115287. [CrossRef]
30. Mashhadi, S.; Homaei, F.; Asadi, A.; Tajammolian, H. Fragility analysis of steel MRFs: Effects of frequency-content components of near-fault pulse-like ground motions and setbacks. *Structures* **2021**, *33*, 3655–3666. [CrossRef]
31. Borhan, S.; Tajammolian, H.; Yazdian, M. Evaluation of seismic performance of rotational-friction slip dampers in near-field and far-filed earthquakes. *Earthq. Struct.* **2021**, *21*, 147–159.

32. Wong, K.K.; Harris, J.L. Seismic damage and fragility analysis of structures with tuned mass dampers based on plastic energy. *Struct. Des. Tall Spec. Build.* **2012**, *21*, 296–310. [CrossRef]

33. Zhang, W.; Liu, S.; Shokrabadi, M.; Dehghanpoor, A.; Taciroglu, E. Nonlinear seismic fragility assessment of tall buildings equipped with tuned mass damper (TMD) and considering soil-structure interaction effects. *Bull. Earthq. Eng.* **2022**, *20*, 3469–3483. [CrossRef]

34. Kircher, C.; Deierlein, G.; Hooper, J.; Krawinkler, H.; Mahin, S.; Shing, B.; Wallace, J. *Evaluation of the FEMA P-695 Methodology for Quantification of Building Seismic Performance Factors*; National Institute of Standards and Technology: Gaithersburg, MD, USA, 2010.

35. OpenSEES. *Open System for Earthquake Engineering Simulation*; University of California: Berkeley, CA, USA, 2008; Available online: https://opensees.berkeley.edu, (accessed on 2 May 2023).

36. Kwong, N.S.; Chopra, A.K.; McGuire, R.K. A ground motion selection procedure for enforcing hazard consistency and estimating seismic demand hazard curves. *Earthq. Eng. Struct. Dyn.* **2015**, *44*, 2467–2487. [CrossRef]

37. Kwong, N.S.; Chopra, A.K.; McGuire, R.K. A framework for the evaluation of ground motion selection and modification procedures. *Earthq. Eng. Struct. Dyn.* **2015**, *44*, 795–815. [CrossRef]

38. Ebrahimian, H.; Jalayer, F.; Lucchini, A.; Mollaioli, F.; Manfredi, G. Preliminary ranking of alternative scalar and vector intensity measures of ground shaking. *Bull. Earthq. Eng.* **2015**, *13*, 2805–2840. [CrossRef]

39. Grigoriu, M. Do seismic intensity measures (IMs) measure up? *Probabilistic Eng. Mech.* **2016**, *46*, 80–93. [CrossRef]

40. Lucchini, A.; Franchin, P.; Mollaioli, F. Uniform hazard floor acceleration spectra for linear structures. *Earthq. Eng. Struct. Dyn.* **2017**, *46*, 1121–1140. [CrossRef]

41. Veismoradi, S.; Cheraghi, A.; Darvishan, E. Probabilistic mainshock-aftershock collapse risk assessment of buckling restrained braced frames. *Soil Dyn. Earthq. Eng.* **2018**, *115*, 205–216. [CrossRef]

42. Ramamoorthy, S.K.; Gardoni, P.; Bracci, J.M. Probabilistic demand models and fragility curves for reinforced concrete frames. *J. Struct. Eng.* **2006**, *132*, 1563–1572. [CrossRef]

43. Ramamoorthy, S.K.; Gardoni, P.; Bracci, J.M. Seismic fragility and confidence bounds for gravity load designed reinforced concrete frames of varying height. *J. Struct. Eng.* **2008**, *134*, 639–650. [CrossRef]

44. Silwal, B.; Ozbulut, O.E. Aftershock fragility assessment of steel moment frames with self-centering dampers. *Eng. Struct.* **2018**, *168*, 12–22. [CrossRef]

45. Hatzigeorgiou, G.D.; Beskos, D.E. Inelastic displacement ratios for SDOF structures subjected to repeated earthquakes. *Eng. Struct.* **2009**, *31*, 2744–2755. [CrossRef]

46. Elkady, A.; Lignos, D.G. Modeling of the composite action in fully restrained beam-to-column connections: Implications in the seismic design and collapse capacity of steel special moment frames. *Earthq. Eng. Struct. Dyn.* **2014**, *43*, 1935–1954. [CrossRef]

47. *NIST 10-917-8*; NIST. Evaluation of the FEMA P-695 Methodology for Quantification of Building Seismic Performance Factors. National Institute of Standards and Technology: Gaithersburg, MD, USA, 2011.

48. *ASCE 7-10*; Minimum Design Loads for Buildings and Other Structures. American Society of Civil Engineers: Reston, VI, USA, 2010.

49. *AISC 360-10*; Specification for Structural Steel Buildings. American Institute of Steel Construction: Chicago, IL, USA, 2020.

50. *AISC 360-16*; Specification for Structural Steel Buildings. American Institute of Steel Construction: Chicago, IL, USA, 2016.

51. Ibarra, L.F.; Medina, R.A.; Krawinkler, H. Hysteretic models that incorporate strength and stiffness deterioration. *Earthq. Eng. Struct. Dyn.* **2005**, *34*, 1489–1511. [CrossRef]

52. *NIST GCR 17-917-46v2*; NIST. Guidelines for Nonlinear Structural Analysis for Design of Buildings Part IIa–Steel Moment Frames. National Institute of Standards and Technology: Gaithersburg, MD, USA, 2017.

53. Feng, D.-C.; Cao, X.-Y.; Wang, D.; Wu, G. A PDEM-based non-parametric seismic fragility assessment method for RC structures under non-stationary ground motions. *J. Build. Eng.* **2023**, *63*, 105465. [CrossRef]

54. Vamvatsikos, D.; Cornell, C.A. Incremental dynamic analysis. *Earthq. Eng. Struct. Dyn.* **2002**, *31*, 491–514. [CrossRef]

55. Kayhan, A.H.; Demir, A.; Palanci, M. Multi-functional solution model for spectrum compatible ground motion record selection using stochastic harmony search algorithm. *Bull. Earthq. Eng.* **2022**, *20*, 6407–6440. [CrossRef]

56. Demir, A.; Palanci, M.; Kayhan, A.H. Evaluation of supplementary constraints on dispersion of EDPs using real ground motion record sets. *Arab. J. Sci. Eng.* **2020**, *45*, 8379–8401. [CrossRef]

57. Baker, J.W.; Cornell, C.A. Which spectral acceleration are you using? *Earthq. Spectra* **2006**, *22*, 293–312. [CrossRef]

58. *ASCE 7-05*; Minimum Design Loads for Buildings and Other Structures. American Society of Civil Engineering: Reston, VI, USA, 2005.